

Analytical and numerical modeling of reconfigurable reflecting metasurfaces with capacitive memory

Abdelghafour Abraray^{1,2}, Diogo Nunes² and Stanislav Maslovski^{1,2}

¹ Instituto de Telecomunicações, Aveiro, Portugal

² Dept. of Electronics, Telecommunications and Informatics, University of Aveiro, Aveiro, Portugal

E-mail: a.abr@av.it.pt, stanislav.maslovski@ua.pt

Abstract. In this article, we develop analytical-numerical models for reconfigurable reflecting metasurfaces formed by chessboard-patterned arrays of metallic patches. These patch arrays are loaded with varactor diodes in order to enable surface impedance and reflection phase control. Two types of analytical models are considered. The first model based on the effective medium approach is used to predict the metasurface reflectivity. The second model is the Bloch wave dispersion model for the same structure understood as a two-dimensional transmission line metamaterial. The latter model is used to study ways to suppress parasitic resonances in finite-size beamforming metasurfaces. We validate the developed analytical models with full-wave numerical simulations. Finally, we outline a design of the metasurface control network with capacitive memory that may allow for independent programming of individual unit cells of the beamforming metasurface.

Keywords: metasurface, high impedance surface, surface impedance, transmission line metamaterial, Bloch waves

1. Introduction

Metasurfaces (MS) are two-dimensional (2D) versions of metamaterials (MM). In the recent years, they attracted a great deal of attention due to unprecedented abilities in manipulating the wavefronts of transmitted and reflected electromagnetic (EM) waves. As compared with the bulk, three-dimensional (3D) MM, MS typically have negligible thickness-to-wavelength ratio. Various MS types have been proposed to transform incident EM radiation in a multitude of ways, with promising realizations at the microwave, terahertz, and optical frequencies [1].

In passive MS, the characteristics of the scattered and transmitted light depend on the geometry, composition and arrangement of the MS meta-atoms or unit cells, which are fixed at the time of manufacturing. Thus, the functionality of such MS cannot be changed once the design is completed. In contrast, with tunable or programmable MS (PMS), one can realize flexible functionalities by dynamically controlling the MS interactions with the incident EM waves, which has a much greater application potential.

Different methods, materials and structures have been proposed to realize tunable MS at microwave frequencies. For example, tunability can be achieved by embedding nonlinear elements such as PIN diodes [2–6], varactor diodes [7, 8], semiconductor or micro-mechanical (MEMS) switches [9], etc. While the reconfigurable PMS for microwave applications are usually controlled electronically, e.g., by varying the bias voltages on the nonlinear elements, there have been proposals to use the visible or infrared light for the MS control [7, 10]. At shorter wavelengths, similar functionalities can be realized by incorporating active or nonlinear material layers into the MS, such as graphene ribbons [11], liquid crystals [12], or phase-change materials (e.g., vanadium dioxide VO₂ [13] and germanium antimony telluride Ge₂Sb₂Te₅ or GST [14]).

Nowadays, there is an emerging trend in using Artificial Intelligence (AI) techniques with the MS designed for high-frequency applications. The use of AI concepts for beamforming and beam tracking applications has been proposed before [15–19]. However, such solutions implemented the neural network algorithms solely in software. Because smart MS can perform practically arbitrary operations on the impinging wave fronts, they can be employed as trainable hardware components in artificial neural networks for beamforming applications [20–23].

MS targeted for applications at the microwaves are traditionally formed by arrays of electrically small elements, which are metal-dielectric structures with the geometry and composition selected carefully in order to generate the needed EM response. In particular, reflecting PMS of different designs have been actively discussed in the literature. Such PMS can be used as controlled reflectors in beamforming antennas. Figure 1 shows the main concept of using reconfigurable reflecting MS in wireless communications.

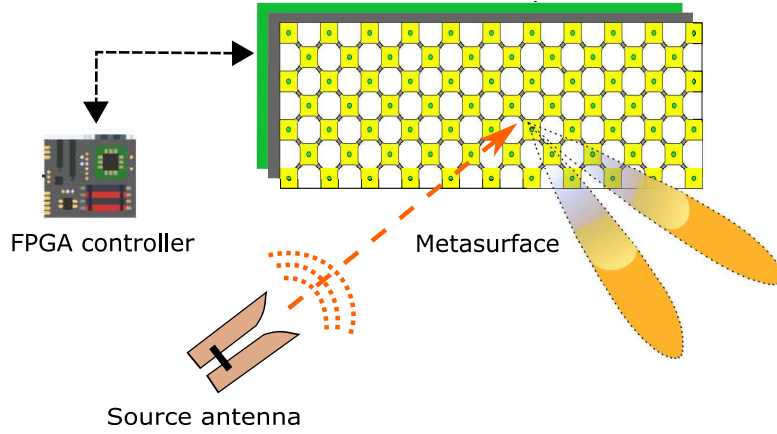


Figure 1. Concept of using reconfigurable reflecting metasurface for beamforming applications.

Due to a high interest in the reconfigurable MS for telecommunication applications, it is important to search for accurate analytical and numerical models of such structures. Because here we will deal with the models of smart reflecting MS, our goal will be to provide a set of analytical and numerical tools suitable for a) modeling the reflection properties of the periodic MS with embedded controlling elements within the framework of the local surface impedance approximation; and b) identifying the parasitic surface mode resonances in such structures and proposing the methods of their suppression. It is hard to underestimate the importance of the surface mode management in the beamforming MS. In fact, an unprecedented level of control over the MS reflection patterns can be achieved with proper “surface mode engineering” techniques that have been developed only relatively recently [24–29].

In this article, we consider a high impedance surface-based (HIS-based) design that utilizes an array of metallic patches with vias placed above a metal plane, similar to the Sievenpiper’s mushrooms [30, 31]. However, we arrange the patches in a chessboard-like structure with the nonlinear capacitive loads (varactors) connected to the neighboring patches at the patch corners. This change in the unit cell geometry allows us to increase the resonant frequency of the HIS. In our structure, the resonant frequency also appears to be stable versus the incidence angle, independently of the incident wave polarization.

An analytical model for such reflecting MS can be developed using a quasistatic model for the uniaxial wire media [32–34] and the additional boundary conditions at the patch-to-via interfaces [35]. However, such models assume that the MS is regular (periodic) in its own plane. In order to account for irregularities (e.g., at the MS edges) we also develop an alternative analytical model based on the dispersion equation for Bloch waves in a two-dimensional (2D) transmission line (TL) metamaterial, with which we study the surface wave excitation and suppression in such MS.

We validate the developed analytical models with numerical simulations in CST Studio Suite and Agilent ADS. In this article we also consider a possible realization of the controlling network that includes capacitors that are used as analog memory to program the MS configuration. Our goal is to keep this network as simple as possible, while realizing independent control of every element of the MS.

2. Analytical model of a periodic varactor-loaded mushroom-type MS

The so-called mushroom-type HIS was first proposed in 1999 by Sievenpiper [30]. Since then analogous designs have been employed in a great number of works (see, for instance, [30, 31, 36, 37]). Mushroom structures can be realized as arrays of metal patches of different shapes (square, hexagonal, Jerusalem crosses, etc.) placed above a grounded dielectric slab (typically, a printed circuit board (PCB) substrate). In such HIS, the patches are connected to the ground by metallic vias passing through the dielectric substrate. The vias operate as an effective wire medium (WM, [33]) layer inserted between the patches and the ground. It can be shown that the WM layer stabilizes the resonant frequency and impedance of the HIS for the waves of transverse magnetic (TM) polarization. The presence of vias is also convenient for realizing loading and controlling networks.

In what follows, we analyze a reflecting MS based on a capacitively-loaded mushroom-type HIS whose top view is depicted in Figure 2. The MS structure shown in this figure is based on a chessboard-like array of square metallic patches with nonlinear capacitive loads (varactors) connected between the corners of the neighboring patches. The array period is a . At the middle of each unit cell, there is a via with radius r_0 that passes through a hole in the ground plane. Below the

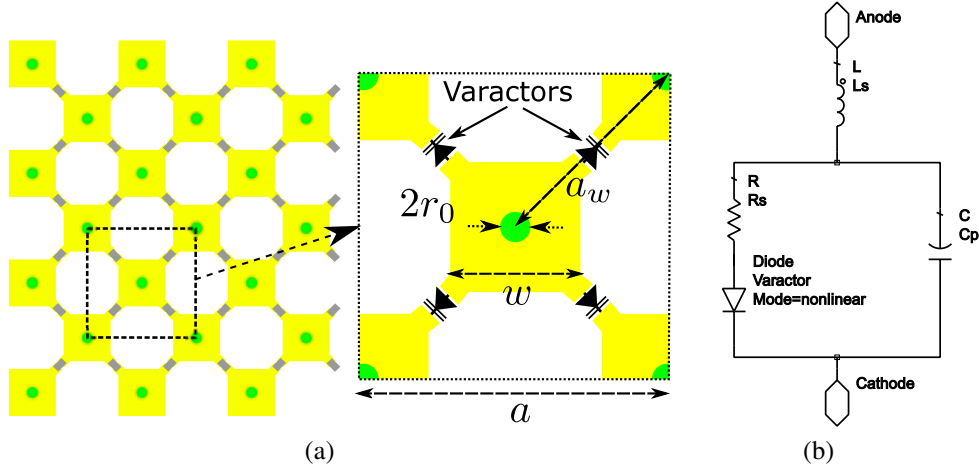


Figure 2. Panel (a): Top view of the chessboard mushroom-type artificial impedance surface with varactor diodes. The green circles mark the vias connecting the square metallic patches to the controlling lines located below the ground plane (not shown). The dashed square delimits a unit cell of the structure, which is also shown in the inset. Panel (b): SPICE model of the varactor diode.

ground plane, this via is connected to a dc bias line (the x -coordinate control line) with negative polarity. Analogously, after passing through holes in the ground plane, the four vias at the corners of the unit cell are connected to the bias lines with positive polarity (the y -coordinate control lines).

In a practical design, the control lines can be formed on a pair of separate metalization layers in a multilayer PCB, or on a separate control PCB located below the ground plane of the HIS structure. In such configuration, the controlling lines do not interfere with the high-frequency fields at the front side of the MS. In order to even better isolate the controlling network from the induced high-frequency currents, one may also place filtering capacitors between the control lines and the HIS ground plane.

From the above description, it is apparent that such a structure can operate as a tunable MS, in which varying voltages applied to the control lines may change the resonant frequencies of the MS unit cells. With a simple modification of the controlling network, one can also make every unit cell of such MS independently programmable by introducing memory capacitors, which will be explained in detail in Section 5.

In the rest of this section, we derive an analytical model for the effective surface impedance and the reflection coefficient for such MS in a linear response regime, i.e., when the amplitude of the high-frequency voltage across the varactors is much smaller than the respective reverse bias voltage. This situation is easily attainable in an MS operating as a tunable reflector in a receiving antenna. This assumption can also hold in low-power transmitting systems.

Under these assumptions, when the period of the MS, a , is small as compared to the wavelength, λ , we may treat the MS as a locally homogeneous periodic structure with some effective surface impedance. This impedance has to be determined from the geometry of the unit cells and the complex impedance of the varactors. By itself, a dense array of disconnected patches acts as an effective capacitive impedance. Due to the induced high frequency currents flowing along the patch edges there exists also an inductive component in the patch grid impedance.

The effective grid capacitance C_g (normalized to ϵ_0) and the inductance L_g (normalized to μ_0) for a simple periodic grid of square patches can be expressed as follows (see, e.g., [37]):

$$C_g = \frac{(\epsilon_r + 1)w \log \csc \frac{\pi(a_e - w)}{2a_e}}{\pi}, \quad L_g = \frac{w \log \csc \frac{\pi(a_e - w)}{2a_e}}{2\pi}, \quad (1)$$

where a_e is the grid period. We have found that these formulas also work well for a chessboard-like grid of patches, if one finds a suitable effective value for a_e . Namely, with a series of numerical tests we have found that the value $a_e = a/2 \pm \delta$, where $\delta \ll a_e$ is a small correction, works quite well for the chessboard-like MS considered in this article. The value of δ can be determined from numerical simulations for the complex reflection coefficient of the MS, by matching the resonant frequency predicted by the analytical model to the one obtained from the simulations. After such a correction is applied, the results of the analytical model are in excellent agreement with the simulation results in a wide frequency range and for arbitrary incidence angles (see Section 3).

Under this approximation, the complex admittance Y_g of the capacitively loaded chessboard-like patch grid

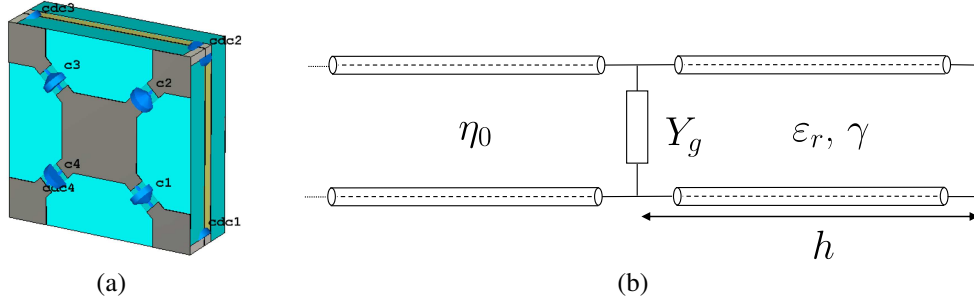


Figure 3. Panel (a): The unit cell of the PMS structure as modeled in SIMULIA CST Studio Suite. Panel (b): TL model for the metal-backed HIS. Here, h is the substrate thickness, ϵ_r is the substrate relative permittivity, $\gamma = \gamma^{TM, TEM, TE}$ is the propagation constant of a given mode, η_0 is the free space impedance, and Y_g is the effective admittance of the patch grid.

(normalized to $\eta_0^{-1} = \sqrt{\epsilon_0/\mu_0}$, where η_0 is the free space impedance), can be expressed as

$$Y_g = \frac{1}{jk_0 L_g + \frac{1}{jk_0 C_g + Y_d}}, \quad (2)$$

where we have taken into account the complex varactor admittance, Y_d (normalized to η_0^{-1}). Because varactors connect the neighboring patches, this admittance is effectively in parallel with the grid capacitance C_g . Here and in what follows, $k_0 = \omega\sqrt{\epsilon_0\mu_0}$ is the free space wavenumber. The admittance Y_d can be obtained from the equivalent SPICE model of the varactor diode [Figure 2(b)]:

$$Y_d = \frac{1}{jk_0 L_s + \frac{1}{jk_0 C_p + \frac{1}{R_s + \frac{1}{jk_0 C_j}}}}, \quad (3)$$

where C_j is the normalized junction capacitance of the varactor diode, C_p is the normalized package capacitance, L_s is the normalized serial inductance, and R_s is the effective serial resistance (normalized to η_0).

Let us first consider the TM incidence. In this case, the normalized surface admittance Y_s^{TM} of the capacitively loaded chessboard-like MS can be obtained with an equivalent TL model shown in Figure 3(b). From this figure it is evident that the admittance Y_s^{TM} is a parallel connection of the surface admittance of the patch grid Y_g and the input admittance of the WM slab Y_{wm} :

$$Y_s^{TM} = Y_{wm} + Y_g. \quad (4)$$

Unlike the typical case of a dielectric slab under the TM incidence, in our situation there are *two* modes propagating inside the uniaxial WM slab formed by the dielectric substrate and the vias: the TM mode and the TEM (transverse electro-magnetic) mode. The complex propagation factors for these waves can be expressed as follows [33]. For the TM wave:

$$\gamma^{TM} = \sqrt{k_t^2 + k_p^2 - \epsilon_r k_0^2}, \quad (5)$$

and for the TEM wave:

$$\gamma^{TEM} = jk_0\sqrt{\epsilon_r}, \quad (6)$$

where $k_t = k_0 \sin \theta$ is the transverse wavenumber (with θ being the angle of incidence), k_p is the WM plasma wavenumber, ϵ_r is the relative permittivity of the substrate. The plasma wavenumber k_p for the uniaxial WM can be approximated as [34]

$$k_p^2 = \frac{2\pi}{a_w^2 \log \frac{a_w^2}{4(a_w - r_0) r_0}}, \quad (7)$$

where $a_w = a/\sqrt{2}$ is the shortest distance between the vias (the WM period).

Next, the normalized input admittance of a uniaxial WM slab, Y_{wm} , with the wires terminated by patches at one side of the slab and connected to the ground at the other side of the slab can be derived by considering the above-mentioned modes and the complete set of boundary conditions (which includes additional boundary conditions, ABCs) at the two sides of the slab, in a manner similar to what was done in [35]. After some algebra, the admittance Y_{wm} , as is seen from the side of the WM slab adjacent to the patch grid, can be expressed as

$$Y_{wm} = \frac{j\epsilon_r k_0 (\kappa \cosh h\gamma^{TM} + \cosh h\gamma^{TEM})}{\kappa\gamma^{TM} \sinh h\gamma^{TM} + \gamma^{TEM} \sinh h\gamma^{TEM}}, \quad (8)$$

where the parameter κ can be expressed as

$$\kappa = \frac{k_t^2 \cosh h\gamma^{TEM} + \alpha\gamma^{TEM} \sinh h\gamma^{TEM}}{k_p^2 \alpha\gamma^{TM} \sinh h\gamma^{TM} + \cosh h\gamma^{TM}}. \quad (9)$$

In these expressions, h is the substrate thickness, and α is the ABC parameter [35]. In this model, we are taking into account the ABC at the connection of vias to the patches, and thus α can be expressed as follows

$$\alpha = \frac{(\varepsilon_r + 1) w \log \frac{a_w^2}{4(a_w - r_0)r_0}}{2\varepsilon_r \log \sec \frac{\pi(a_e - w)}{2a_e}}. \quad (10)$$

On the other hand, the same admittance can be approximated by considering only the TEM waves in the WM slab and neglecting the TM waves (which are evanescent when $\sqrt{\varepsilon_r}k_0 < k_p$). Under this approximation, the normalized input admittance Y_s^{TEM} reads

$$Y_s^{TEM} = Y_g - j\sqrt{\varepsilon_r} \cot(\sqrt{\varepsilon_r}k_0h). \quad (11)$$

Let us now consider the transverse electric (TE) incidence. In this case, the only modes existing in the WM slab are the TE waves with the complex propagation factor

$$\gamma^{TE} = \sqrt{k_t^2 - \varepsilon_r k_0^2}, \quad (12)$$

because under the TE incidence the thin vias practically do not interact with the incident electric field (because it is perpendicular to the vias). Thus, for the TE incidence, the normalized input admittance can be written as

$$Y_s^{TE} = Y_g + \frac{\gamma^{TE} \coth(\gamma^{TE}h)}{jk_0}. \quad (13)$$

Finally, the electric field reflection coefficient for the cases of the TM and TE incidence can be defined by using the full model as

$$R_s^{TM} = \frac{1 - Y_s^{TM} \cos \theta}{1 + Y_s^{TM} \cos \theta}, \quad R_s^{TE} = \frac{1 - Y_s^{TE} / \cos \theta}{1 + Y_s^{TE} / \cos \theta}. \quad (14)$$

Alternatively, when using the simplified model for the TM case,

$$R_s^{TM} = \frac{1 - Y_s^{TEM} \cos \theta}{1 + Y_s^{TEM} \cos \theta}. \quad (15)$$

The simplified model can be used for validation of the complete model at the frequencies where the TM mode in the WM has no effect.

3. Numerical modeling of the PMS equipped with a control board

In order to validate the analytical model, we have simulated the considered PMS structure in the commercial EM full-wave simulation software SIMULIA CST Studio Suite. In addition, in the numerical simulations we have considered a more realistic structure that included a control board that is placed at the back of the HIS.

As it was mentioned before, the considered PMS can be formed by a pair of PCBs: the frontside board that realizes the mushroom-type HIS, and the backside board with the x and y control lines. We have built one period of such a structure (the unit cell) in the 3D modeler of the SIMULIA CST Studio Suite. Realistic material models for the PCB substrates (Isola IS680 with the thickness $h = 1.52$ mm and the relative permittivity $\varepsilon_r = 3.38$, $\tan \delta = 0.002$) and metalization layers (annealed copper with thickness $t = 35$ μm , $\sigma = 5.8 \times 10^7$ S/m) have been used. A view of the unit cell of this structure as realized in SIMULIA CST Studio Suite is shown in Figure 3(a). The two PCBs are separated by a gap of 0.5 mm filled with epoxy resin ($\varepsilon_r = 4$). The period of the MS was $a = 6.8$ mm and the patch size was $w = 3$ mm. The varactor diodes were modeled with a lumped LCR equivalent circuit resulting from the SPICE model of the varactor diode [Figure 2(b)], whose capacitance was changed depending on the studied case, which corresponded to changing the varactor diode control voltage. The unit cell model also included the filter capacitors connected at the points where the vias pass through the ground plane of the front-side PCB.

The unit cell was placed under the Floquet-periodic boundary conditions and the incident plane wave propagating at an angle with respect to the z -axis (normal to the MS) was modeled by using a Floquet port. The Floquet modes that simulated the incident waves consisted of two orthogonally polarized plane waves. The reflection amplitude and phase for these incident waves were recorded as functions of frequency and the incidence angle.

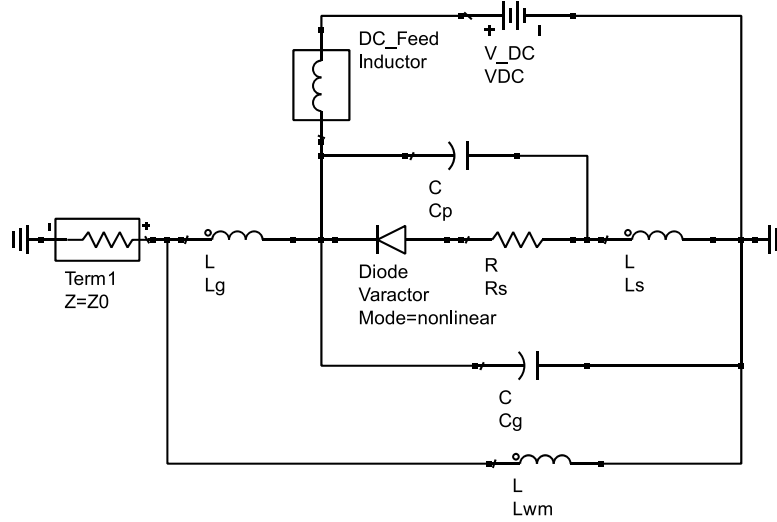


Figure 4. Equivalent circuit model of the varactor-loaded unit cell as realized in Agilent ADS.

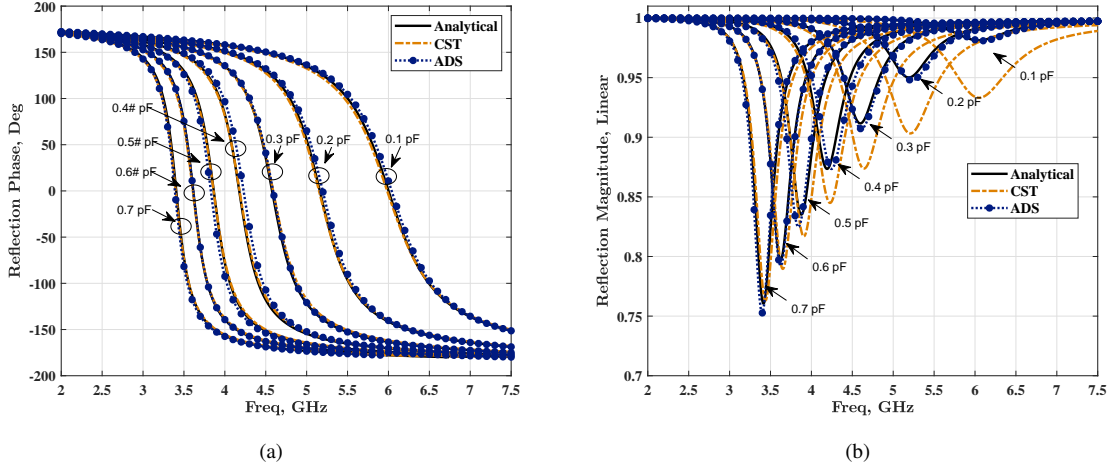


Figure 5. Complex reflection coefficient versus frequency for different values of the junction capacitance corresponding to the varactor diode MAVR-000120-1141. Panel (a): Reflection phase. Panel (b): Reflection magnitude. The varactor diode has the serial inductance $L_s = 0.2$ nH, serial resistance $R_s = 0.88$ Ohm, and package capacitance $C_p = 0.14$ pF. Under the control voltage variation from 0 to $V_b = 20$ V (the breakdown voltage) the junction capacitance C_j varies from about 1 to 0.1 pF. The curves are obtained with the correction parameter $\delta = 0.3$ mm. The equivalent parameters of the diode were confirmed by vector-network analyzer (VNA) measurements.

The MS unit cell model was also simulated using Agilent ADS. In ADS, the MS unit cell can be modeled with an equivalent circuit dictated by the structure of Eqs. (2), (3), and (4). The ADS circuit was formed by an effective inductance $L_{wm} = \eta_0 / (\omega_0 \text{Im} Y_{wm}|_{\omega_0})$ modeling the WM layer (here, $\omega_0 = 2\pi f_0$, with f_0 being the desired central frequency) connected in parallel to a circuit modeling the loaded patch grid that comprised a lumped capacitor $C = \epsilon_0 C_g$, an inductor $L = \mu_0 L_g$, [Eq. (1)], and a varactor diode represented by its SPICE model (Figure 4).

The phase of the reflection coefficient under normal incidence obtained from the analytical model and from the CST and ADS simulations is shown in Figure 5 for different capacitor values. By decreasing the capacitance value from 0.7 to 0.1 pF, the resonant frequency can be tuned over a range from about 3.4 to 6 GHz. For each value of the capacitance, the reflection phase varies with the range of about 360° and crosses through zero at the resonant frequency of the MS, where it behaves as an artificial magnetic conductor, because close to the resonant frequency the input impedance of the MS is very high. In order to achieve efficient control of the reflected wavefront, the reflection phase should ideally cover the full 360° range.

Dependence of the reflection phase on frequency for the same MS structure has been also studied under oblique

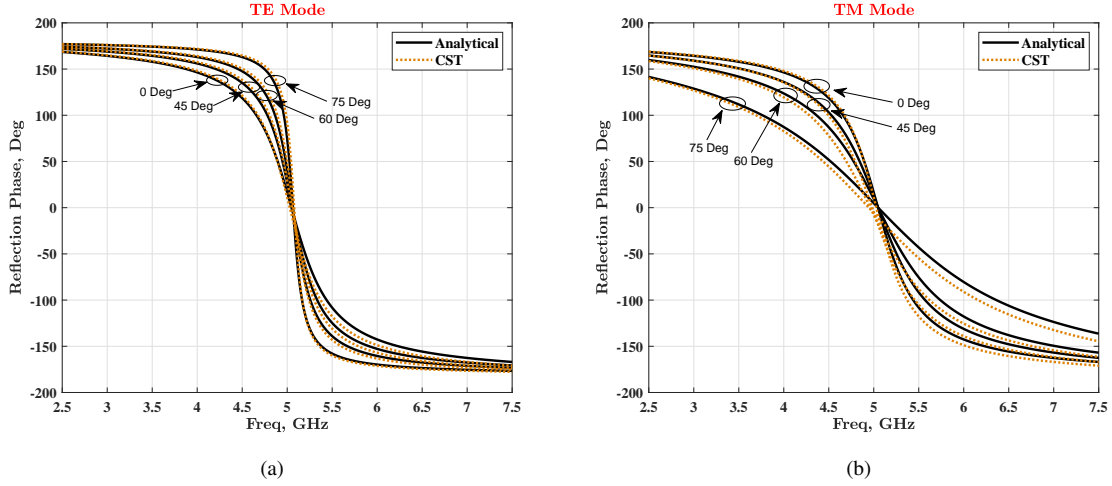


Figure 6. Reflection phase versus frequency for different values of the incidence angle. Panel (a): TE incidence. Panel (b): TM incidence.

incidence. The corresponding results for the case when the HIS resonates at about 5 GHz are presented in Figure 6, from which one can see that although the behavior is different for the TE and TM polarizations, the reflection phase curves for all incidence angles cross zero at approximately the same frequency. The resonance bandwidth decreases for the TE polarization and increases for the TM polarization as the angle of incidence grows, as expected. Thus we may conclude that the studied structure has robust performance with respect to the incident wave polarization and the angle of incidence. In all studied cases, the results of the analytical model agreed very well with the numerical simulation results. The numerical simulations also confirmed that the control board placed behind the HIS has no effect on the performance of the HIS at the microwave frequencies.

4. Nonuniformities and parasitic Bloch waves on finite mushroom-type HIS

The analytical model developed in the previous section is valid only for a uniform MS with equal unit cells distributed periodically over a very large (theoretically, infinite) area. However, because the beamforming operation requires varying the local surface impedance over the MS in a complex way, the beamforming PMS generally cannot be uniform from the EM point of view. Realistic PMS also have finite dimensions. Therefore, complementary models or extended models are needed to describe such generally nonuniform PMS.

There have been successful attempts on modeling MS with periodic geometries and with nonuniform distributions of surface impedance among the unit cells. In general, treatment of such structures requires considering coupling between the Floquet harmonics of the field scattered by the MS. Beamforming techniques based on such approaches allow for a full control over the radiation pattern of a reflecting MS [24–29]. Because the higher-order Floquet harmonics are similar to resonating surface modes supported by periodic structures, one may say that beamforming in such structures is realized via proper surface mode engineering. In theory, patterns with arbitrary main beam directions and low sidelobe levels can be achieved with such techniques.

However, and especially in finite-size PMS that comprise many complex unit cells, the surface mode engineering problem may become very complex, with many influencing factors that might be overlooked by the available analytical-numerical models. For example, the surface impedance-based models that have a very good accuracy when dealing with the plane wave incidence and reflection, may become rather inaccurate when dealing with non-uniformly excited realistic MS. Indeed, realistic HIS include several dielectric and metalization layers. Thus such complex structures may support additional modes that propagate in these layers. The finite size of the unit cells also makes the local surface impedance models inaccurate due to the spatial dispersion effects that are prominent when the wavelength becomes comparable to the unit cell size.

In this section we are going to investigate the surface modes that exist in the finite-size chessboard-like mushroom structures. This study was motivated by unwanted phenomena that we observed when we numerically simulated finite MS samples with the unit cell shown in Figure 3(a). Namely, in those simulations we observed excitation of parasitic modes produced by irregularities at the edges. An efficient approach to tackle such effects in the finite-size structures can be

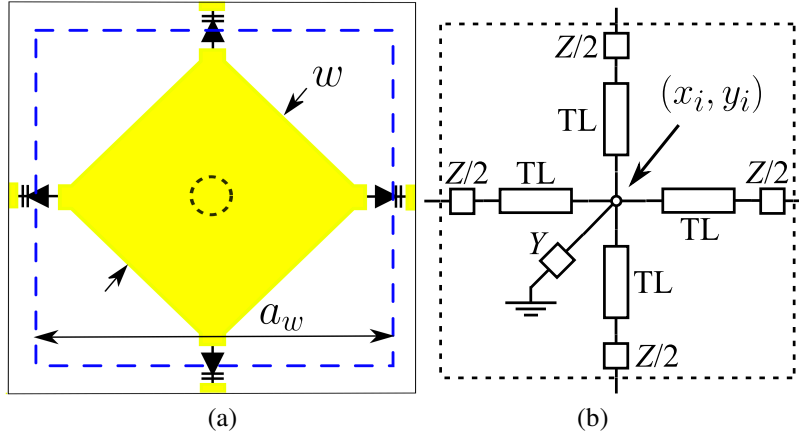


Figure 7. Panel (a): Reduced 45°-rotated unit cell of the chessboard structure (inside the dashed square). Panel (b): Schematic of the corresponding TL-based 2D metamaterial.

devised by using the Bloch wave dispersion theory for the 2D TL-based metamaterials [38].

Let us consider a finite MS sample formed by equal unit cells terminated at the MS edges with some impedances that we need to determine. In order to suppress the parasitic resonating modes, we may use the fact that when the termination impedance equals the characteristic impedance of the unwanted mode, the reflections at the MS edges are suppressed and the parasitic resonances disappear.

To find the dispersion and the impedance of the MS-supported parasitic modes understood as the Bloch waves in a 2D-periodic TL-based metamaterial we consider the equivalent circuit of the reduced, 45°-rotated unit cell shown in Figure 7. In the equivalent circuit of this cell, the admittance Y is formed by a parallel connection of the via's inductance L_{via} to the ground [32],

$$L_{via} = \frac{\mu_0 h \log \frac{a_w^2}{4r_0(a_w - r_0)}}{2\pi}, \quad (16)$$

and the effective patch capacitance to the ground, C_{pat} , given by

$$C_{pat} = \frac{\varepsilon_0 \varepsilon_r w^2}{h} + C_0, \quad (17)$$

where the additional capacitance, C_0 , is the self-capacitance of a patch in the periodic array of patches [34]:

$$C_0 = \frac{\varepsilon_0 \pi w (\varepsilon_r + 1)}{\log \sec \frac{\pi(a_e - w)}{2a_e}}. \quad (18)$$

From these results, the shunt admittance Y that connects every patch to the common ground reads

$$Y = \frac{1}{j\omega L_{via}} + j\omega C_{pat}. \quad (19)$$

The serial impedance Z represents the small-signal complex impedance of a varactor diode that can be obtained from the SPICE model of the diode: $Z = \eta_0 Y_d^{-1}$, where Y_d is given by Eq. (3).

Due to the 45° rotation of the unit cell, the surface waves that impinge on the MS edges at the right angle have $|k_{x'}| = |k_{y'}|$ in the rotated coordinate system (x', y') of the reduced unit cell shown in Figure 7. Taking this fact into account, the resulting dispersion equation can be written as [38]:

$$k_{x'} = \pm a_w^{-1} \cos^{-1} \left[\frac{YZ}{8} + \cos(\beta_0 a_w) \left(1 + \frac{YZ}{8} \right) + \frac{j}{2} \sin(\beta_0 a_w) \left(\frac{Z}{Z_0} + \frac{YZ_0}{2} \right) \right]. \quad (20)$$

Note that the dispersion equation for the Bloch waves is qualitatively different from the dispersion equation for the surface waves on a homogenized mushroom layer (for example, compare it with Eq. (20) from [36]). Nevertheless, we will soon see that the location of the propagation band predicted by the Bloch model coincides with the one predicted by the dispersion equation for the TM-polarized surface waves, $k_t = k_0 \sqrt{1 - (1/Y_s^{TM})^2}$, [36]. Indeed, near the resonance of the HIS, $1/Y_s^{TM} \rightarrow \pm i\infty$ and thus $k_t \gg k_0$, from which one may conclude that the surface waves must appear near

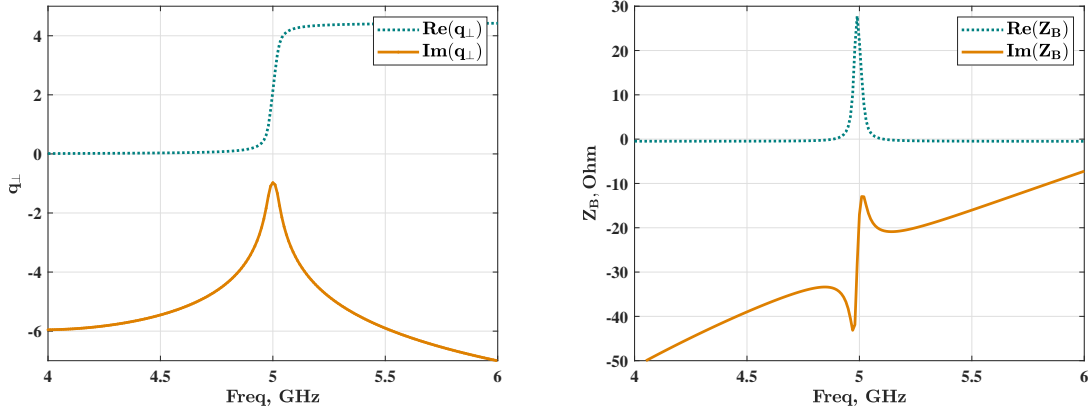


Figure 8. Panel (a): Dispersion of the Bloch waves, where $q_{\perp} = k_{\perp} a_{wm}$ is the normalized propagation factor. Panel (b): Bloch wave impedance Z_B as a function of frequency.

the HIS resonance. However, in addition to the dispersion characteristics, the Bloch wave approach allows us to find the required termination impedance, as is shown next.

In Eq. (20), Z_0 is the reference TL impedance and $\beta_0 = k_0 \sqrt{\epsilon_r}$ is the TL propagation factor. The propagation factor in the direction orthogonal to an MS edge is $k_{\perp} = k_{x'} \sqrt{2}$. Thus, the Bloch impedance Z_B for the respective surface modes reads [38]

$$Z_B = \pm \left(Z_0 \tan \frac{\beta_0 a_w}{2} - \frac{jZ}{2} \right) \cot \frac{k_{\perp} a_w}{2\sqrt{2}}, \quad (21)$$

where the sign must be chosen so that $\text{Re}(Z_B) > 0$.

To estimate the deteriorating effect of the resonant Bloch modes excited on the PMS, we have modeled finite MS samples with the unit cell size and other parameters as in the previous calculations for the infinite periodic MS. For the purpose of the Bloch impedance and dispersion calculations, the reference impedance Z_0 was estimated from the substrate parameters and the width of the top metalization at the points where the varactors are connected to the patches: $Z_0 = 71.6 \, \Omega$, by using the standard formulas for microstrip lines. The varactor diode model used in the following studies was characterized with the serial inductance $L_s = 0.2 \, \text{nH}$, the serial resistance $R_s = 0.88 \, \Omega$, and the package capacitance $C_p \approx 0.14 \, \text{pF}$. The varactor junction capacitance was set to $C_j = 0.2 \, \text{pF}$ in order to obtain the HIS resonance at around 5 GHz.

The obtained dispersion of the parasitic Bloch waves is plotted in Figure 8(a), and the Bloch impedance as a function of frequency is shown in Figure 8(b). It can be seen that our qualitative analytical model predicts existence of the propagating Bloch waves near 5 GHz, with the real part of the Bloch impedance close to 20–30 Ohm in the middle of the band. Based on these results, we conclude that in order to suppress the unwanted surface mode resonances, one has to add terminating resistors. One possibility is to add such resistors at the connections of the vias to the ground plane at the edges of the MS. Because at such edge the x' - and y' -directed currents of the rotated unit cells (Figure 7) add up, the terminating resistance must be set to $Z_B/2$. Because the impedance varies within the band, a roughly average value of $Z_B/2 \approx 11 \, \Omega$ was selected.

To demonstrate effectiveness of the terminating resistors for suppression of parasitic modes, we have numerically simulated several finite-size MS samples in SIMULIA CST Studio Suite. Some characteristic results are shown in Figure 9 before and after adding the termination resistors. From Figure 9(a) one can see that in the MS sample without the terminating resistors the parasitic modes are excited in the frequency range close to 5 GHz, which affects the phase distribution over the MS. One may also notice the unwanted resonances at the frequencies below 5 GHz, which are not immediately accounted by the qualitative model. However, from Figure 9(b) one can see that all parasitic resonances disappear in the finite MS sample with the terminating resistors. This confirms that the proposed method of parasitic mode suppression with the terminating resistance obtained from the Bloch wave model is viable and effective.

5. Design and modeling of the controlling network with capacitive memory

In this section we describe an extension to the controlling network formed by the x and y bias lines that allows us to set up the varactor bias voltages individually for each unit cell of the MS. In order to achieve this functionality, we add a memory

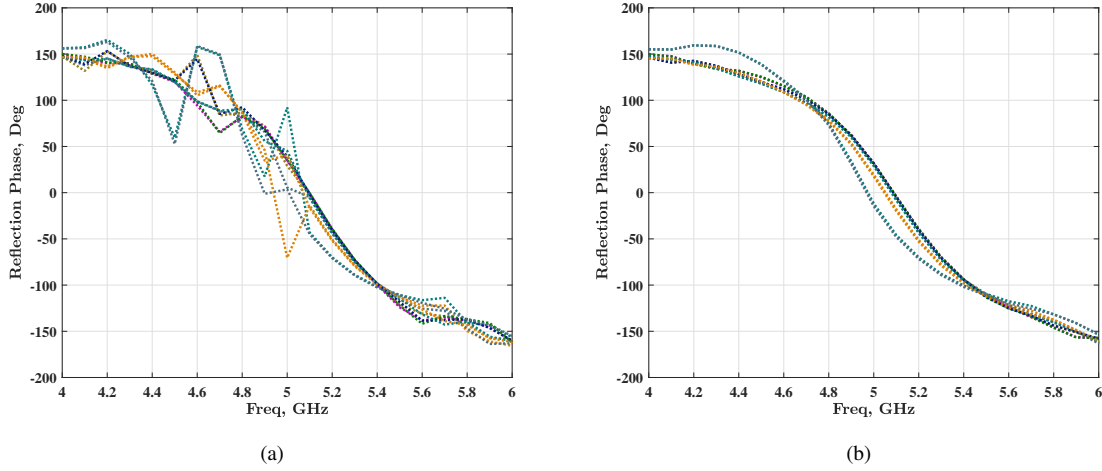


Figure 9. Parasitic mode suppression in a finite-size MS formed by 3×10 unit cells (SIMULIA CST Studio Suite simulation; several curves are for the local reflection phases at different unit cells). Panel (a): The phase performance of the finite-size MS before adding the $Z_B/2$ terminating resistors. Panel (b): The phase performance of the finite-size MS after adding the $Z_B/2$ terminating resistors.

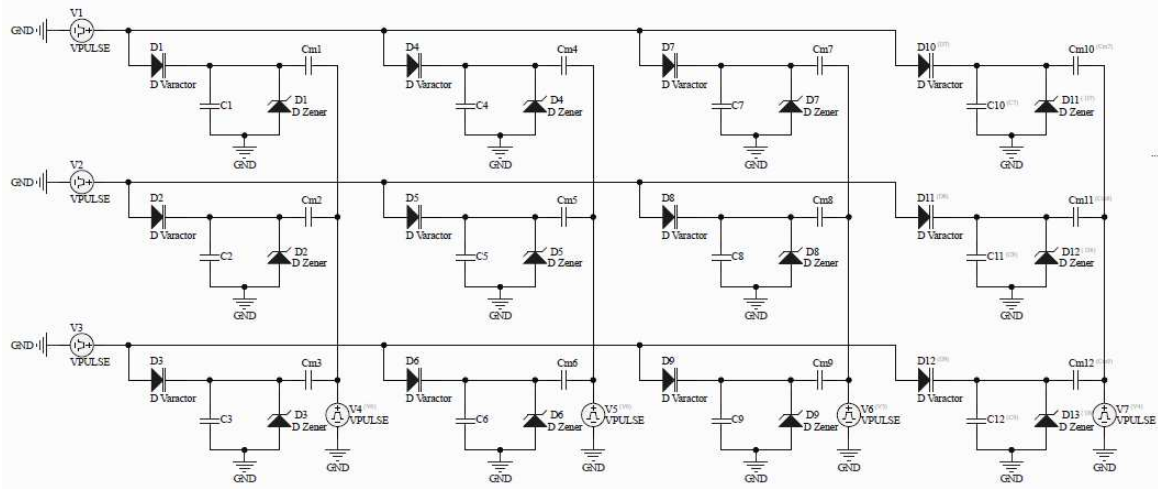


Figure 10. Controlling network with capacitive memory as modeled in ADS.

capacitor to each unit cell, as is explained next.

The extended controlling network with capacitive memory is depicted in Figure 10. As compared to the basic bias network in which the anodes of the varactors are simply connected to the x bias lines and the cathodes to the y bias lines, in the extended network we introduce additional memory capacitors $C_{m,i}$, $i = 1, 2, \dots$ (one per unit cell), which are inserted between the y controlling lines and the vias leading to the varactor's cathodes [the corner via in Figure 2(a)]. Note that in the equivalent network shown in Figure 10, a single diode symbol represents a pair of varactors from the original MS, because these varactors are effectively connected in parallel with each other at dc and share the same bias voltage. In the same equivalent network, we also present the filter capacitors C_i , the purpose of which is to prevent the high-frequency currents from flowing into the rest of the bias network.

As can be seen from Figure 10, at the intersection of the control lines the varactor diode and the memory capacitor are connected in such a way that when the varactor diode is forward-biased the memory capacitor gets charged through the open diode (the programming phase), and when the polarity is opposite the memory capacitor keeps its charge and the voltage on this capacitor (in addition to the standby voltage on the control lines) determines the dynamic capacitance of the varactor and thus the resonant frequency of the unit cell. The Zener diodes are included in this network to be able to discharge the memory capacitors by applying high voltage pulses with inverse polarity to the y -lines. As we will show next, with such bias network topology we are able to control each cell separately, which means that more freedom

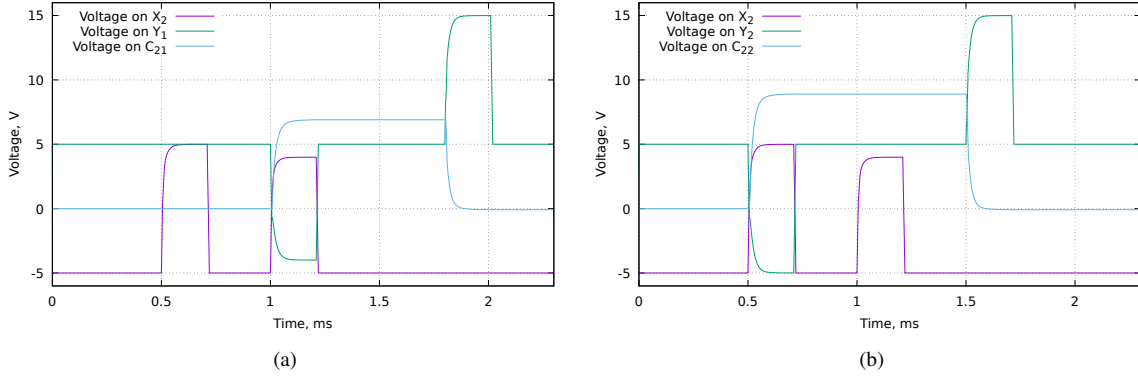


Figure 11. Panel (a): Voltages on the X2 and Y1 lines and the memory capacitor C_{21} . Panel (b): Voltages on the X2 and Y2 lines and the memory capacitor C_{22} . The memory capacitor values are $C = 1$ uF, and the characteristic charging/discharging time is on the order of RC , where $R = 50$ Ohm are the current limiting resistors connected to all control lines (not shown in Figure 10).

in manipulating the local surface impedance and the reflection phase is available.

The programming of this PMS with capacitive memory can be accomplished by applying appropriate pulsed voltage to the structure, in which the memory capacitors are repeatedly charged to a certain capacity, or discharged through the Zenner diodes with erasing pulses. The time-domain signal analysis of such programming and erasing processes has been carried out by using Agilent ADS. In the simulations we have considered the circuit from Figure 10 that includes a 3-by-4 network of the control lines that we name X1, X2, X3 (the horizontal lines, counted from the top) and Y1, Y2, Y3, Y4 (the vertical lines, counted from left to right).

In Figure 11(a) we plot the simulated voltages on the X2 and Y1 lines and on the memory capacitor $C_{m,2} = C_{21}$ belonging to the (2, 1)-th unit cell, and in Figure 11(b) we show the voltages on the X2 and Y2 lines and on the capacitor $C_{m,5} = C_{22}$ in the (2, 2)-th unit cell. As one can see, the coincident voltage pulses of opposite polarity on the lines X2 and Y2 (starting at $t = 0.5$ ms) charge the memory capacitor in the (2, 2)-th cell (programming phase). At the same time, the (2, 1)-th cell is not affected. Analogously, the coincident voltage pulses on the lines X2 and Y1 (starting at $t = 1$ ms) program the (2, 1)-th unit cell, and the (2, 2)-th cell is not affected. One may also note that the programmed voltage on the memory capacitors can be adjusted by varying the amplitudes of the voltage pulses on the X and Y lines. That is why the programmed voltages on C_{21} and C_{22} are different. Finally, the erasing high voltage pulses starting at $t = 1.5$ ms and $t = 1.8$ ms on the Y1 and Y2 lines discharge the memory capacitors connected to the respective lines. Note that the entire columns of unit cells connected to these lines can be erased independently.

To conclude, we have confirmed that the proposed implementation of the control network with memory capacitors enables independent programming of unit cells of the PMS. Additionally, the proposed schematic reduces component cost because here the varactors combine the functions of diode switches and controllable capacitive loads.

6. Conclusions

In this study, a number of analytical and numerical methods to analyze reconfigurable Sievenpiper mushroom-type PMS equipped with varactors and memory capacitors have been developed. We have used these methods to propose and investigate a PMS structure suitable for microwave applications at the frequencies from 3.6 to 6 GHz (e.g., for the future 5G+ systems). The unit cell design and the control network topology proposed in this article enable independent programming of all unit cells of the PMS.

The analytical model developed in Section 2 has been used to predict the surface impedance and the complex reflectivity of the considered PMS for the TE and TM incidence cases with a high accuracy. In Section 3, the analytical results have been validated with the full-wave numerical simulations in SIMULIA CST Studio Suite for a wide range of frequencies and incidence angles. Additionally, a simplified equivalent circuit model has been developed and tested in Agilent ADS. The results of the analytical and numerical models are in very good agreement and demonstrate potential benefits of using the studied structures for the beamforming and beam steering applications. In particular, the proposed chessboard-like PMS has shown excellent stability of the resonant frequency with respect to the incidence angle for both TE and TM polarizations.

In Section 4, we have developed a qualitative analytical model for the parasitic resonant surface modes on the finite-size mushroom-type PMS. With this model, we have been able to determine the optimal value of the terminating resistors

that have to be added to the unit cells at the edges of the structure in order to suppress unwanted resonances and recover the expected beamforming behavior of the PMS.

In Section 5, we have proposed and studied the controlling network suitable for the considered PMS. In such network, the controlling voltage in the form of short bipolar pulses is applied to the unit cells through a network of disconnected x and y control lines and a set of memory capacitors. We have performed a number of circuit simulations in order to determine optimal parameters of the network and the amplitude and the duration of the programming and erasing pulses applied to the coordinate lines. The obtained results have confirmed the validity of our designs.

The theoretical models and practical concepts developed in this article will find applications in the actively developing areas of research and technology that deal with reconfigurable metasurfaces for future telecommunication systems.

Acknowledgment

This work has been funded by Fundação para a Ciência e a Tecnologia (FCT), Portugal, under the Carnegie Mellon Portugal Program (project ref. CMU/TIC/0080/2019).

References

- [1] Glybovski S B, Tretyakov S A, Belov P A, Kivshar Y S and Simovski C R 2016 *Phys. Rep.* **634** 1–72
- [2] Cui T J, Qi M Q, Wan X, Zhao J and Cheng Q 2014 *Light: Sci. & Appl.* **3** e218
- [3] Wan X, Qi M Q, Chen T Y and Cui T J 2016 *Sci. Rep.* **6** 35692
- [4] Li L, Cui T J, Ji W, Liu S, Ding J, Wan X, Li Y B, Jiang M, Qiu C W and Zhang S 2017 *Nat. Comm.* **8** 197
- [5] Li Y B, Li L L, Xu B B, Wu W, Wu R Y, Wan X, Cheng Q and Cui T J 2016 *Sci. Rep.* **6** 23731
- [6] Yang H, Cao X, Yang F, Gao J, Xu S, Li M, Chen X, Zhao Y, Zheng Y and Li S 2016 *Sci. Rep.* **6** 35692
- [7] Zhang X G, Tang W X, Jiang W X, Bai G D, Tang J, Bai L, Qiu C W and Cui T J 2018 *Adv. Sci.* **5** 1801028
- [8] Zhang X G, Jiang W X and Cui T J 2018 *Appl. Phys. Lett.* **113** 091601
- [9] Ren Z, Chang Y, Ma Y, Shih K, Dong B and Lee C 2019 *Adv. Opt. Materials* **8** 1900653
- [10] Shadrivov I V, Kapitanova P V, Maslovski S I and Kivshar Y S 2012 *Phys. Rev. Lett.* **109** 083902
- [11] Soleymani S, Güngördü M Z, Kung P and Kim S M 2019 *Sci. Rep.* **9** 1249
- [12] Wang Q, Zhang X G, Tian H W, Jiang W X, Bao D, Jiang H L, Luo Z J, Wu L T and Cui T J 2019 *Adv. Theory and Simulations* **2** 1900141
- [13] Cai H, Chen S, Zou C, Huang Q, Liu Y, Hu X, Fu Z, Zhao Y, He H and Lu Y 2018 *Adv. Opt. Materials* **6** 1800257
- [14] Pogrebnikov A V, Bossard J A, Turpin J P, Musgraves J D, Shin H J, Rivero-Baleine C, Podraza N, Richardson K A, Werner D H and Mayer T S 2018 *Opt. Mat. Express* **8** 2264
- [15] Hougne P, Imani M F, Diebold A V, Horstmeyer R and Smith D R 2019 *Adv. Sci.* **7** 1901913
- [16] Southall H, Simmers J and O'Donnell T 1995 *IEEE Trans. Antenn. Propagat.* **43** 1369–1374
- [17] Zooghyby A E, Christodoulou C and Georgiopoulos M 2000 *IEEE Trans. Antenn. Propagat.* **48** 768–776
- [18] Du K L, Lai A, Cheng K and Swamy M 2002 *Signal Processing* **82** 547–561
- [19] Rawat A, Yadav R and Shrivastava S 2012 *AEU - Int. J. of Electronics and Communications* **66** 903–912
- [20] Maslovski S, Abraray A, Carvalho N and Navarro A 2020 *Proc. of International Congress on Engineered Material Platforms for Novel Wave Phenomena – Metamaterials*, (New York, United States) 225–227, doi:10.1109/Metamaterials49557.2020.9285085
- [21] Abraray A, Navarro A, Carvalho N and Maslovski S 2021 *Proc. of 2021 Telecoms Conference (ConfTELE)*, (Leiria, Portugal) 1–6, doi:10.1109/ConfTELE50222.2021.9435548
- [22] Abraray A and Maslovski S 2021 *Proc. of Fifteenth International Congress on Artificial Materials for Novel Wave Phenomena – Metamaterials* (New York, United States) 257–259, doi:10.1109/Metamaterials52332.2021.9577063
- [23] Kaboutari K, Abraray A and Maslovski S, 2021 *Proc. of International Conference on Electrical Engineering and Photonics (EExPolytech)* (St. Petersburg, Russia) 63–66, doi:10.1109/EExPolytech53083.2021.9614934
- [24] Di Renzo M, Zappone A, Debbah M, Alouini M-S, Yuen C, De Rosny J and Tretyakov S 2020 *IEEE J. on Selected Areas in Communications* **38**(11) 2450–2525
- [25] Díaz-Rubio A, Asadchy V S, Elsakka A and Tretyakov S A 2017 *Sci. Adv.* **3** e1602714
- [26] Díaz-Rubio A and Tretyakov S A 2021 *IEEE Trans. Antenn. Propagat.* **69**(10) 6560–6571
- [27] Ra'di Y, Sounas D and Alú A 2017 *Phys. Rev. Lett.* **119** 067404
- [28] Ra'di Y and Alú A 2022 *IEEE Photonics J.* **14**(1) 1–13
- [29] Ra'di Y and Alú A 2018 *ACS Photonics* **5** 1779
- [30] Sievenpiper D and Zhang L *et al.* 1999 *IEEE Trans. Microw. Theory and Techn.* **47**(11) 2059–2074
- [31] Sievenpiper D and Schaffner J *et al.* 2003 *IEEE Trans. Antenn. Propagat.* **51**(10) 2713–2722
- [32] Maslovski S I, Tretyakov S A and Belov P A 2002 *Microw. Opt. Technol. Lett.* **35** 47–51
- [33] Belov P A, Marqués R, Maslovski S I, Nefedov I S, Silveirinha M, Simovski C R and Tretyakov S A 2003 *Phys. Rev. B* **67** 113103
- [34] Maslovski S I and Silveirinha M G 2009 *Phys. Rev. B* **80** 245101
- [35] Maslovski S, Morgado T A, Silveirinha M G, Kaipa C S R and Yakovlev A 2010 *New J. Phys.* **12** 113047
- [36] Yakovlev A, Silveirinha M *et al.* 2009 *IEEE Trans. on Microw. Theory and Techn.* **57**(11) 2700–2714
- [37] Tretyakov S 2003 *Analytical modeling in applied electromagnetics* (Norwood, MA: Artech House, Inc.)
- [38] Maslovski S I, Ferreira H R L, Medvedev I O and Brás N G B 2018 *Phys. Rev. B* **98** 245143